




Original Article

Acute Mechanical Consequences of Vessel-Specific Coronary Bypass Combinations

COLTON J. KOSTELNIK,¹ MARY K. GALE,² KIERSTEN J. CROUSE,³ TAREK SHAZLY,^{1,3} and JOHN F. EBERTH ^{1,4}

¹Biomedical Engineering Program, University of South Carolina, Columbia, SC, USA; ²Biomedical Engineering Department, Georgia Institute of Technology, Atlanta, GA, USA; ³Mechanical Engineering Department, University of South Carolina, Columbia, SC, USA; and ⁴Biomedical Engineering, Science and Health Systems, Drexel University, Philadelphia, PA, USA

(Received 2 September 2022; accepted 6 February 2023; published online 24 February 2023)

Associate Editor James E. Moore oversaw the review of this article.

Abstract

Purpose—Premature coronary artery bypass graft (CABG) failure has been linked to geometric, mechanical, and compositional discrepancies between host and graft tissues. Acute hemodynamic disturbances and the introduction of wall stress gradients trigger a myriad of mechanobiological processes at the anastomosis that can be associated with restenosis and graft failure. Although the origins of coronary artery disease dictate the anastomotic target, an opportunity exists for graft-vessel optimization through rationale graft selection.

Methods—Here we explored the four distinct regions of the left (L) and right (R) ITA (1 = proximal, 2 = submuscular, 3 = middle, 4 = distal), and four common target vessels in the coronary circulation including the proximal and distal left anterior descending (PLAD & DLAD), right coronary (RCA), and left circumflex (LCX) arteries. Benchtop biaxial mechanical data was used to acquire constitutive model parameters of these tissues and enable vessel-specific computational models to elucidate the mechanical consequences of 32 unique graft-target combinations.

Results—Simulations revealed the maximum principal wall stresses for the PLAD, RCA, and LCX occurred when anastomosed with LITA₁, and the maximum flow-induced shear stress occurred with LITA₄. The DLAD, on the other hand, reached stress maximums when anastomosed to LITA₄. Using a normalized objective function of simulation output variables, we found LITA₂ to be the best graft choice for both LADs, RITA₃ for the RCA, and LITA₃ for the LCX.

Conclusion—Although mechanical compatibility is just one of many factors determining bypass graft outcomes, our data

suggests improvements can be made to the grafting process through vessel-specific regional optimization.

Keywords—Vascular biomechanics, Histomechanics, Finite element analysis (FEA), Computational fluid dynamics (CFD).

INTRODUCTION

Advanced coronary artery disease often requires surgical bypass using autologous vessels to reestablish adequate blood flow to the heart. Despite new surgical techniques, materials, and interventional criteria that have improved overall patency, the 1st-year failure rates for coronary artery bypass grafting (CABG) remain between 5 and 15% and are strongly dependent upon the source tissue.^{16, 17, 34} Vein grafts, for example, suffer from progressive intimal-medial hyperplasia with only a 65% 5-year patency rate.³⁰ Although the etiology of vein-graft disease is multifactorial, due partly to their mechanical composition and microstructure, it has been hypothesized that veins exposed to altered hemodynamic loading induce endothelial cell damage, thrombosis, and fibrosis.^{10, 11} Concurrent with this is the concept of structural mechanical mismatching (compliance mismatching) at the anastomotic junction—a location of vulnerability in the grafting process^{5, 17, 22, 46}—which is a consequence of both geometrical and mechanical differences between the host and graft tissues.^{6, 16, 22, 44} The sudden change in deformed vessel geometry across the anastomotic junction can also cause atherogenic flow

Address correspondence to John F. Eberth, Biomedical Engineering, Science and Health Systems, Drexel University, Philadelphia, PA, USA. Electronic mail: jfe28@drexel.edu

disturbances around contraction and expansion points^{12, 13, 18} triggering endothelial conformational and functional changes.^{1, 8} Likewise, mechanosensitive mural cells that guide regulatory, remodeling, and migratory pathways, may experience altered wall stresses near the anastomotic junction and exhibit an unfavorable cellular response.^{19, 24, 33} Overall, graft-host mechanical and geometric mismatching present a major risk of graft failure and restenosis.^{7, 9}

Arteries, especially the internal thoracic artery (ITA), have been used successfully in bypass grafting; thus, the pathology of artery graft failure has received less attention than veins. The left (LITA) and right (RITA), for example, possess abundant histomechanical similarities to the left anterior descending artery (LAD), supporting its continued use as the superior autograft option.^{15, 17, 20, 34} Moreover, the single anastomotic junction and native hemodynamic similarity improve overall patency. Our recent investigation revealed that the ITA exhibits multiple histological patterns depending on the distance from the heart (i.e., elastic, hybrid, muscular), and can be divided into four distinct anatomical grafting regions (1 = proximal, 2 = submuscular, 3 = middle, 4 = distal).^{15, 26, 29, 42} Likewise, coronary arteries and their branches possess distinct regional variations in geometry and microstructure that can change with sex, age, species, and disease conditions.^{25, 43}

In this study, we quantified the properties of four different coronary artery targets, namely the proximal and distal left anterior descending (PLAD & DLAD), right coronary artery (RCA), and left circumflex artery (LCX), using the American Yorkshire pig as a surrogate for the human central vasculature. Histomechanical results were directly compared to those of the middle LITA segment (LITA₃) to serve as a representative sample of ITA architecture.^{21, 38} Biaxial mechanical data was used to estimate constitutive modeling parameters using a nonlinear, hyperplastic, structurally motivated material model within a continuum mechanics framework. Leveraging these data, idealized computational models of end-to-end anastomoses with 32 different graft-target (ITA-coronary) combinations were constructed.²⁶ Finite Element Analyses (FEA) were first used to simulate and perform a “virtual anastomosis” through alignment of the vessel’s lumens and attachment of the two tissues. Finally, the resultant deformed geometry was fed into a Computational Fluid Dynamics (CFD) simulation to model fluid-flow behavior. Although end-to-end anastomosis is not the preferred surgical configuration, computational models were designed to mimic ongoing mechanobiological laboratory experiments and provide an initial indication of source tissue performance. Given that the bypass region (e.g., PLAD, DLAD,

RCA, LCX) is dictated by the clinically determined stenosis location, a normalized objective function, based on mechanical deviation from homeostatic stresses, was found for each graft-coronary combination so that the preferred ITA region could be selected for each coronary target.

MATERIALS AND METHODS

Tissue Acquisition

Porcine coronary arteries and ITAs were acquired from 2-year-old American Yorkshire sows from a local abattoir weighing approximately 200 kg. All arteries were dissected under sterile conditions within 1 h of slaughter and transported in 1% phosphate-buffered saline (PBS) with heparin sodium (20 units/mL), cleaned, and separated into different groups for histological and mechanical characterization (Fig. 1). The four coronary arteries included the proximal and distal left anterior descending artery (PLAD & DLAD), right coronary artery (RCA), and left circumflex artery (LCX). Where applicable, and for simplicity purposes, the discrete histological ($n = 5$, each) and mechanical data ($n = 4$, each) were averaged for each group of coronary arteries. These averaged values were compared to the average histological ($n = 4$) and mechanical ($n = 5$) values of the third segment of the left ITA (LITA) excised from the same pigs. Our previous work revealed this segment had the fewest notable differences from other segments of the left or right ITA.²⁶

Biaxial Mechanical Testing

All testing was performed on fresh arteries and completed within 48 h of animal sacrifice. Before performing acute biaxial mechanical testing on our Bose BioDynamic biaxial mechanical testing device, the region of each coronary artery to be tested underwent a rigorous selection process to ensure accurate and reproducible results. The region that exhibited the least amount of twisting or bending was selected for biaxial testing with an average undeformed length of ~ 9.88 mm and an angle of $\geq 164^\circ$ (straight = 180°) for all coronary arteries. These vessels were mounted onto two Luer fittings and fixed in place by tying several 3–0 braided sutures around the ends. An initial measurement of the unloaded length was recorded as the distance between sutures, which aided in calculating experimental axial stretch ratios. The tissue samples were submerged in the testing bath and perfused with 1% PBS and sodium nitroprusside (10^{-5} M) to elicit a fully passivated state. Vessels were inflated to pre-de-

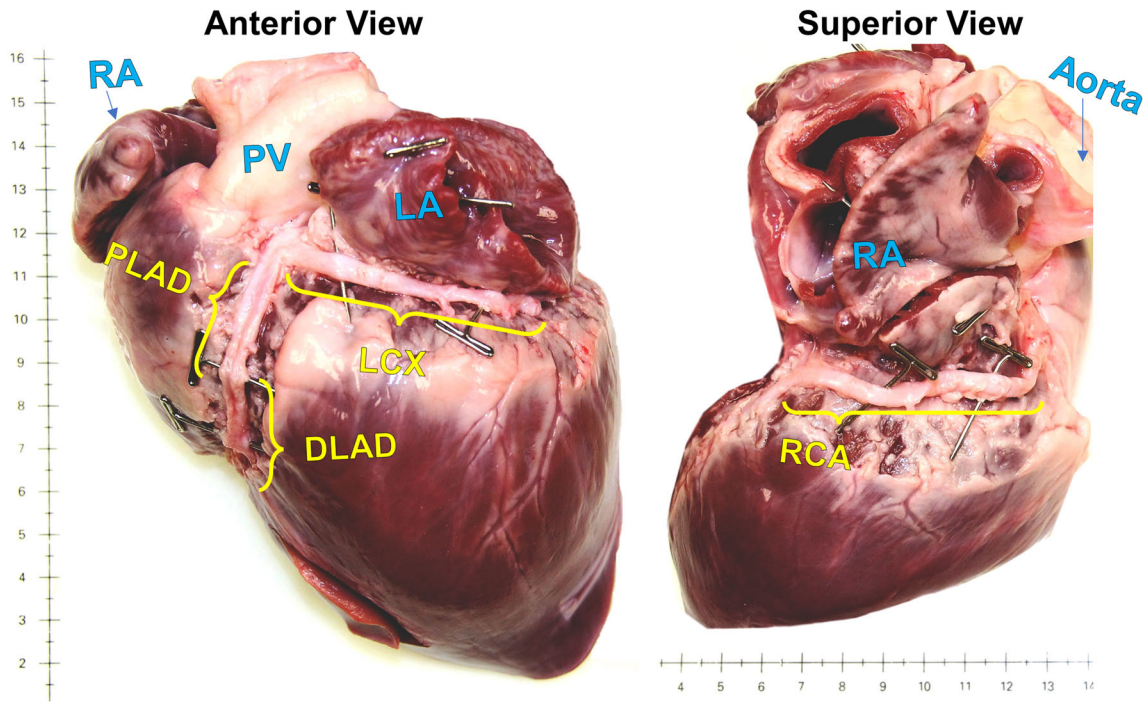


FIGURE 1. Porcine heart from the anterior and superior view with distinct structures labeled to discern relative sizes and locations of the four coronary arteries of interest. *PLAD* proximal left anterior descending artery; *DLAD* distal left anterior descending artery; *LCX* left circumflex artery; *RCA* right coronary artery; *RA* right atrium; *LA* left atrium; *PV* pulmonary vein.

finer pressures by increasing the volumetric flow rate and the downstream resistance, per the design of the testing device. Every sample underwent five cycles of axial extension and inflation preconditioning to minimize viscous dissipation and ensure reproducible results. Inflation-extension testing was then conducted at 0–200 mmHg and at three axial stretch ratios, the *in vivo* stretch, and $\pm 10\%$. The *in vivo* axial stretch ratio was the axial extension which yielded a constant force measurement during changes in pressure. The luminal pressure and axial displacement were both controlled while the deformed outer radius and axial force were recorded.

Following biaxial mechanical testing, a 1 mm thick ring segment was cut from the middle of the vessel, and a cross-sectional image was captured. The residual strain in the vessel was removed by making a radial cut and allowing the tissue to equilibrate for 30 min in 1% PBS. An image of this zero-stress state was captured using a Canon EOS 60d DSLR camera mounted to a dissecting microscope using an adapter lens (Micro Tech Lab). ImageJ image analysis software (NIH) was used to measure the geometries of both images. The unloaded thickness and opening angle were calculated from

$$H = \frac{2A}{L_i + L_o} \quad (1)$$

and

$$\Phi = \pi - \frac{L_o - L_i}{2H}, \quad (2)$$

where L_i and L_o are the inner and outer arc lengths, respectively, and A the cross-sectional area. Under the assumption of incompressibility, the inner radius at any deformed state could be calculated as

$$r_i = \sqrt{r_o^2 - \frac{A}{\pi\lambda_z}}, \quad (3)$$

where λ_z is the axial stretch ratio. The mid-wall circumferential and axial stretches can be calculated from

$$\lambda_\theta = \frac{2\pi(r_i + r_o)}{L_i + L_o}, \quad (4)$$

$$\lambda_z = \frac{l}{L}, \quad (5)$$

where l and L are the deformed and undeformed lengths, respectively. Then the mean circumferential stress, mean axial stress, and area compliance are calculated from

$$\sigma_\theta = \frac{Pr_i}{h}, \quad (6)$$

$$\sigma_z = \frac{F}{\pi(r_o^2 - r_i^2)}, \quad (7)$$

$$C_A = \pi \frac{\Delta r_i^2}{\Delta P}, \quad (8)$$

where F is the axial force, P the transmural pressure, and h the wall thickness. For area compliance, Δr_i^2 is the change in inner radius squared (area) per change in pressure ΔP calculated around a 100 ± 20 mmHg operating point.

Constitutive Modeling of Experimental Data

The constitutive modeling framework was identical to our previous investigation with extended details and procedures found therein.²⁶ Briefly, we used a modified version of the structurally-motivated constitutive model proposed by Holzapfel, Gasser, and Ogden to include the four families of collagen fibers^{4, 23} to represent each coronary artery uniquely, so that

$$W(\mathbf{C}, \mathbf{M}^k) = \frac{c}{2}(I_C - 3) + \sum_{k=1}^4 \frac{c_1^k}{4c_2^k} \left\{ \exp \left[c_2^k (IV_C^k - 1)^2 \right] - 1 \right\}, \quad (9)$$

where $I_C = \text{tr}(\mathbf{C})$ and $IV_C^k = \mathbf{M}^k \cdot \mathbf{C} \mathbf{M}^k$ are the first and fourth principal invariants, respectively of the right Cauchy–Green deformation tensor, \mathbf{C} . $\mathbf{M}^k = [0, \sin(\alpha^k), \cos(\alpha^k)]$ is a unit vector oriented in the direction of the k th fiber at an angle α^k relative to the axial direction with $\alpha^1 = 0$, $\alpha^2 = \pi/2$, and $\alpha^3 = -\alpha^4$. Assuming relatively small radial stresses, the problem is reduced to plane stress and the theoretical pressure and force calculated from

$$P' = \frac{h}{r_i} \left[\lambda_\theta \frac{\partial W}{\partial \lambda_\theta} - \lambda_r \frac{\partial W}{\partial \lambda_r} \right], \quad (10)$$

$$F' = \pi h (2r_i + h) \left[2\lambda_z \frac{\partial W}{\partial \lambda_z} - \lambda_r \frac{\partial W}{\partial \lambda_r} \right]. \quad (11)$$

The eight-independent positive modeling parameters were then found by least-squares minimization of an objective function between the experimentally measured [Eqs. (6)–(8)] and theoretically modeled [Eqs. (10)–(11)] values of pressure and force using MATLAB's optimization toolbox (MathWorks; Natick, MA).

Computational Modeling

To simulate outputs from both the solid and fluid domains, computational models of each possible grafting configuration were generated for all 32 coronary-ITA combinations in FEBio.²⁷ The experimentally determined material properties were represented using the available constitutive model for a solid mixture of anisotropic four fiber families embedded in an isotropic ground matrix. In all cases, the ITA's unloaded inner diameter was greater than the coronary artery so the lumens were first matched by applying an equal but opposite direction pressure to the inner surface elements at the ends of the respective vessels until a continuous lumen was formed. Then a tied facet-on-facet contact was enforced between the two arteries to serve as a “virtual anastomosis” with approximated geometry. A fixed displacement boundary condition for the z -direction was applied to the non-anastomosed ends of both the graft and coronary arteries. For simplicity, the virtually anastomosed tissues were studied under a single quasi-static inflation pressure of 100 mmHg. Thus, the previous step's stress history was not carried to the final simulation. The magnitude of the first principal stress (σ_1 —maximum normal stress in a plane oriented to be absent of shear) for each anastomosis was found and plotted vs. location along the graft-coronary axis. The displacement tolerance, energy tolerance, and line search tolerance for this solid mechanical FEA model were set to 0.001, 0.01, and 0.9, respectively. The simulation results were deemed mesh-independent if mesh refinement led to less than a 0.5% change in the average first principal stress.² A total of 7680 hexahedral (hex8) elements were required for mesh independence.

The inflated lumen mesh at 100 mmHg was extracted to build a computational fluid dynamics (CFD) model to simulate steady and fully developed blood flow through the anastomosis consisting of a 10 mm long segment of the ITA graft on the proximal side and a 10 mm segment of the coronary artery on the distal side. Blood was modeled as an incompressible non-Newtonian Carreau fluid ($\eta_0 = 0.25$ Pa s; $\eta_\infty = 0.0035$ Pa s; $\lambda_b = 25$; $n = 0.25$) with a fluid density of 1060 kg/m³ and zero-slip fluid boundary conditions applied to the outer surface of the extracted geometry representing the interface between the blood and the arterial wall.^{3, 28} Additionally, a zero fluid dilation boundary condition was applied to the inlet and outlet surfaces. Because direct blood flow measurements were not feasible with abattoir-sourced pigs, published coronary blood flow data from young, healthy domestic swine were used to calculate the volumetric flow of each coronary artery using allometric scaling laws.³² For simplicity, analyses were

performed under steady flow conditions, so the effects of the fluid–solid interface and vessel wall motion were not analyzed. The tissues were then used to predict regional maximum fluid shear stress (τ_w —wall stress due to fluid friction acting opposite to the direction of blood flow) across the anastomoses in the *in vivo*-like loaded condition. The fluid velocity tolerance, fluid dilatation tolerance, and energy tolerance within the CFD model were set to 0.001, 0.001, and 0.01, respectively. CFD simulation outputs were deemed mesh-independent if additional mesh refinement led to less than a 0.5% change in the average fluid shear stress.² A total of 155,159 tetrahedral (tet4) elements were required to reach mesh independence.

Since blood vessels have a preferred homeostatic or “basal” state of stress,^{24, 33} the maximum σ_1 values from the solid mechanical model were normalized to basal coronary σ_1 values taken from biaxial mechanical data captured at the force-invariant axial stretch and 100 mmHg. Likewise, the maximum τ_w values from the fluid dynamic model were normalized to basal τ_w values. The basal coronary stresses were given a value of 0, and the maximum stresses from each model were given a value of 1 to scale the anastomosis configurations in terms of the most significant deviation from basal coronary stresses (GraphPad Prism).

Histological Analysis

Fresh arteries were fixed in 4% paraformaldehyde and embedded in paraffin wax. Sections were cut at 5 μm and stained with Movat’s Pentachrome or Picrosirius Red (PSR). Tissue segments from the same heart were processed together to facilitate a uniform histological comparison. Brightfield images were then obtained using a Nikon E600 microscope and computer interface with Q Capture (QImaging). The PSR stained sections were imaged through brightfield microscopy and cross-polarized light using a Zeiss AxioCam MCr5. Each arterial cross-section was imaged around the vessel’s circumference at five different locations.

Constituent area fractions were obtained using ImageJ software with the “Threshold_Colour” plugin. Movat’s Pentachrome stained sections were used to estimate area fractions of elastin and smooth muscle cells (SMCs). On the other hand, the area fraction of collagen was found as the ratio of PSR cross-polarization birefringence to the total tissue measured in the brightfield. The standard threshold values were fixed at specified brightness, saturation, and hue ranges to ensure experimental consistency. Elastin was stained deep red/brown and was quantified using a bandpass filter from brightness 34–155 and saturation 60–255, and a band stop filter from hue 4–130. SMCs were

stained red/pink and were quantified using a bandpass filter from brightness 135–220, saturation 90–185, and hue 0–11. The sums of these areas were normalized to 1 for each sample. Cross-polarized light analysis of collagen birefringence was quantified separately for the medial and total cross-sectional areas. The medial region of interest (ROI) was confined to the inner and outer elastic lamellae area. The total birefringence signal was measured using a bandpass filter from brightness 30–255, saturation 0–255, and hue 0–255.

Statistical Analyses

Experimental data were analyzed using GraphPad Prism to identify the statistical significance of discrete metrics of LITA and the coronary vasculature. Comparisons of the mechanical properties were conducted through a one-way ANOVA with a two-tailed paired *t*-test of unequal variances. The histological data were analyzed through a two-way ANOVA in conjunction with two-tailed paired *t*-tests of unequal variances to determine statistical differences between the amounts of load-bearing constituents found within the arterial samples. Statistically significant differences were taken at confidence levels of $p < 0.05$, $p < 0.01$, and $p < 0.001$.

RESULTS

Plots are displayed for all coronary arteries at their respective force-invariant stretch (middle) as well as $\pm 10\%$ stretch (low, high) (Fig. 2). The axial force-pressure profiles revealed that the force-invariant stretch for the DLAD was the only artery that maintained a force reading above 0.5 N for the entire experimental pressure range. The pressure-outer diameter profiles exhibited some of the expected variability commonly observed when using abattoir tissue samples. However, the circumferential stress and stretch measurements had comparatively smaller error bars due to their calculation’s dependency on each specimen’s cross-sectional area or unloaded radius, respectively. From this data, the structurally-motivated constitutive model revealed a set of best-fit parameters that demonstrated an excellent fit to grouped experimental data (Table 1) with an average root mean square error (RMSE) of 0.2405 across all coronary arteries. Since the reported parameters are fitted for the grouped data, rather than fitted for an individual sample and then averaged, values are reported without standard deviation and no statistical comparisons are made. Nevertheless, we note that the isotropic parameter *c* was highest for the PLAD and lowest for the RCA making up 48.9 and 10.2%,

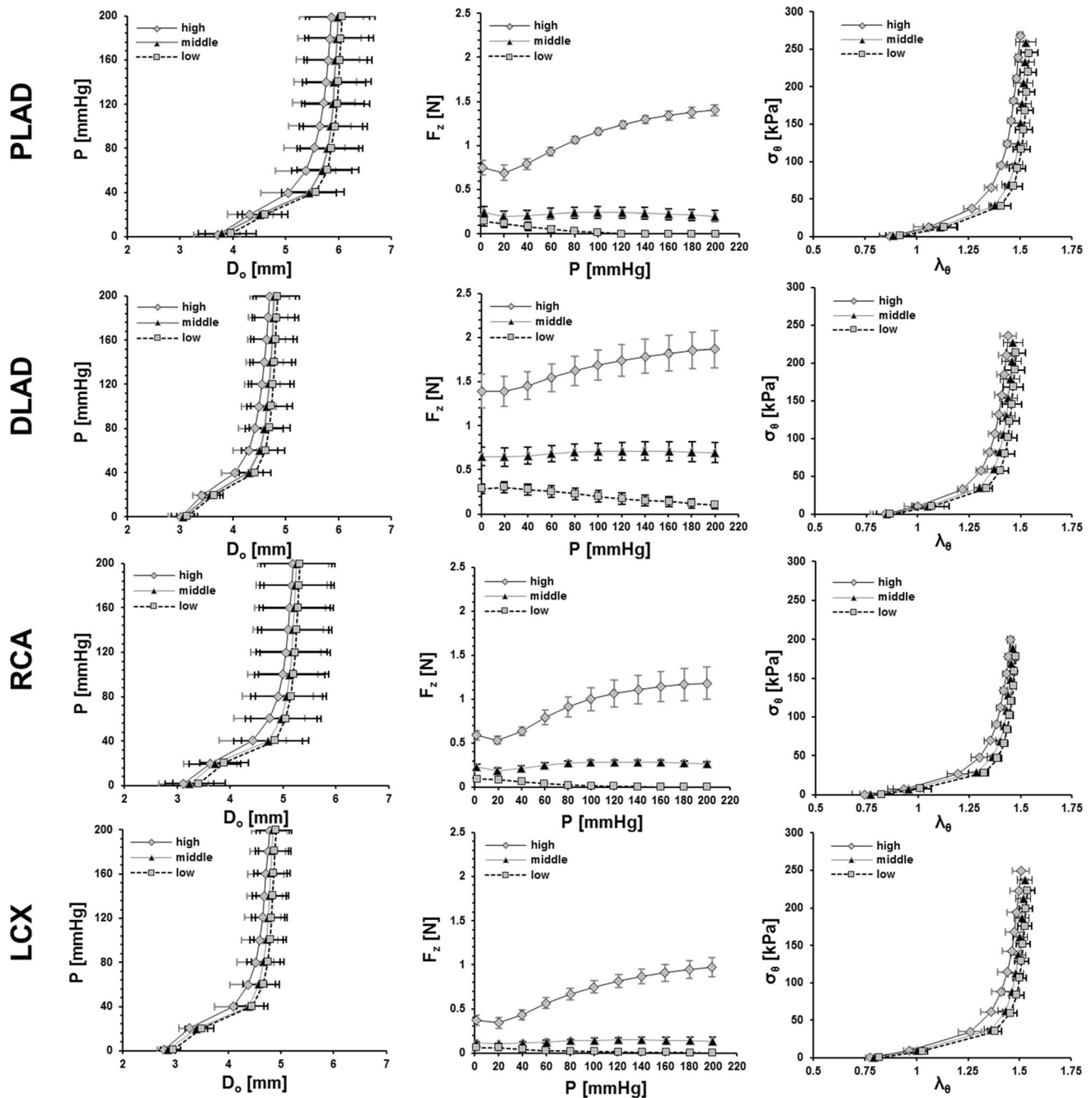


FIGURE 2. Biaxial mechanical data of the four porcine coronary arteries ($n = 4$, each). The leftmost plots are pressure–outer diameter data, the center plots are axial force–pressure data, and the rightmost plots are mean circumferential stress–mid-wall circumferential stretch data. Data was collected at three distinct stretch ratios, the force-invariant stretch (middle) as well as $\pm 10\%$ strain (low, high). Mean \pm SEM.

respectively, of the total elastic energy when assessed at *in vivo*-like stretch conditions. Likewise, the paired contribution of the anisotropic parameters, c_1 and c_2 , to the total strain energy for the DLAD is much higher in the axial (superscript 1, 41.6% of the total) than in the circumferential direction (superscript 2, 10.8% of the total) when assessed at *in vivo* conditions. By comparison, the axial and circumferential contribu-

tions to the total strain energy of the LCX were 17.9 and 16.9%, respectively.

Data captured from the stress-free configurations revealed that LITA has significant geometric differences from the coronary arteries (Table 2). The LITA outer arc length was significantly larger than the PLAD ($p = 0.039$), DLAD ($p < 0.001$), RCA ($p = 0.001$), and LCX ($p < 0.001$), while the LITA

TABLE 1. Fitted material parameters for grouped coronary artery datasets used in this study.

Coronary artery	c (kPa)	c_1^1 (kPa)	c_2^1	c_1^2 (kPa)	c_2^2	$c_1^{3,4}$ (kPa)	$c_2^{3,4}$	α (rad)	RMSE
PLAD	14.70	8.122	1.696	1.564	1.955	1.451	3.025	0.707	0.280
DLAD	10.80	47.87	1.197	1.215	2.231	3.395	2.850	0.666	0.099
RCA	1.278	5.372	1.883	2.905	1.675	4.177	2.310	0.644	0.276
LCX	4.966	4.762	2.605	1.306	2.067	5.493	2.315	0.653	0.307

TABLE 2. Averaged unloaded geometries for each group of ($n = 4$) arteries.

Blood vessel	Unloaded thickness [H] (mm)	Inner arc length [L_i] (mm)	Outer arc length [L_o] (mm)	Opening angle [Φ] ($^\circ$)
PLAD	0.595 ± 0.080	13.03 ± 1.209	$12.36 \pm 1.112^*$	$218.8 \pm 14.06^*$
DLAD	0.502 ± 0.097	$9.750 \pm 1.208^*$	$9.599 \pm 1.024^*$	$183.8 \pm 44.09^*$
RCA	0.636 ± 0.123	10.87 ± 2.944	$10.257 \pm 2.365^*$	$204.2 \pm 51.17^*$
LCX	0.504 ± 0.022	$9.731 \pm 1.141^*$	$9.210 \pm 1.192^*$	$216.9 \pm 12.13^*$
LITA	0.512 ± 0.091	14.34 ± 1.385	16.20 ± 2.213	78.93 ± 59.35

Mean \pm SD.

*Signifies statistical significance between coronary arteries and LITA₃ using one-way ANOVA at $p < 0.05$.

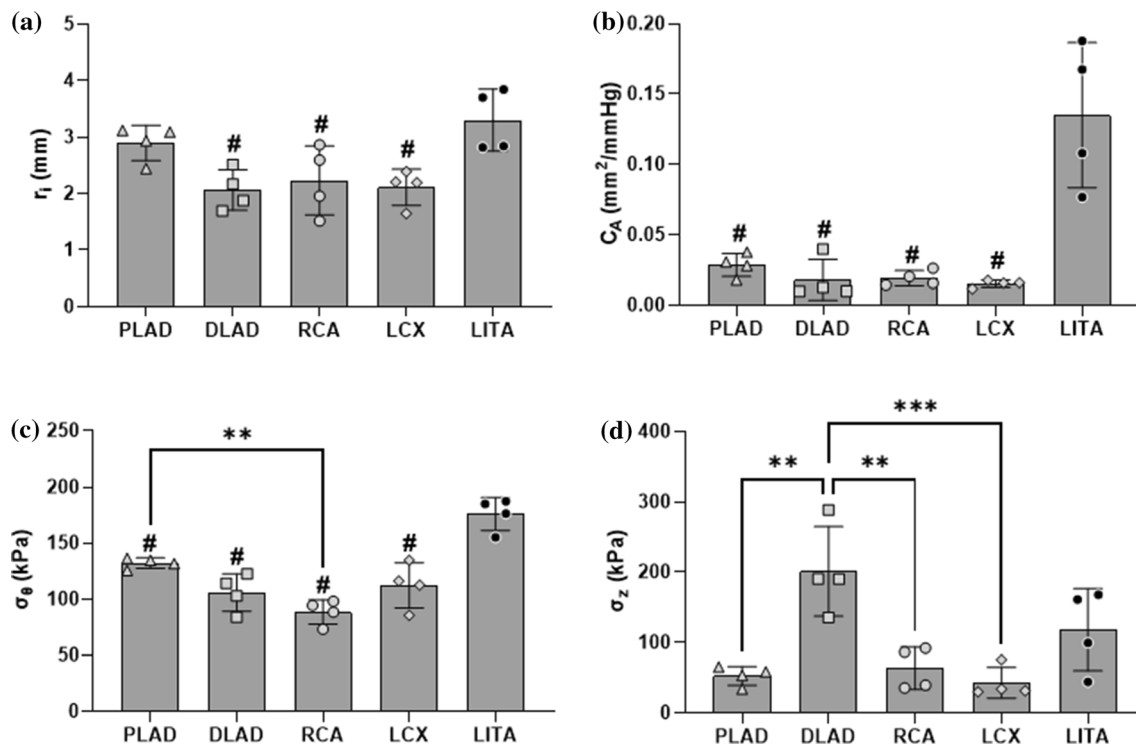


FIGURE 3. Biaxial mechanical data of the porcine coronary arteries and the third LITA segment plotted at common loading conditions of 100 mmHg and the force-invariant stretch ($n = 4$, each). (a) Inner radius; (b) area compliance; (c) circumferential stress; (d) axial stress. Statistical significance between different coronary arteries is indicated by () and (***) at $p < 0.01$ and $p < 0.001$, respectively. Statistical significance between a coronary artery and LITA is indicated by (#) at $p < 0.05$. Mean \pm SD.**

opening angle was significantly smaller than the PLAD ($p = 0.003$), DLAD ($p = 0.021$), RCA ($p = 0.005$), and LCX ($p = 0.004$). Comparing mechanical data at common loading conditions (i.e., 100 mmHg, force-invariant axial stretch) revealed that LITA has a sig-

nificantly larger loaded inner radius than DLAD ($p = 0.010$), RCA ($p = 0.029$), and LCX ($p = 0.014$) (Fig. 3a). Similarly, LITA exhibited significantly larger area compliance ($p < 0.001$) and circumferential stress

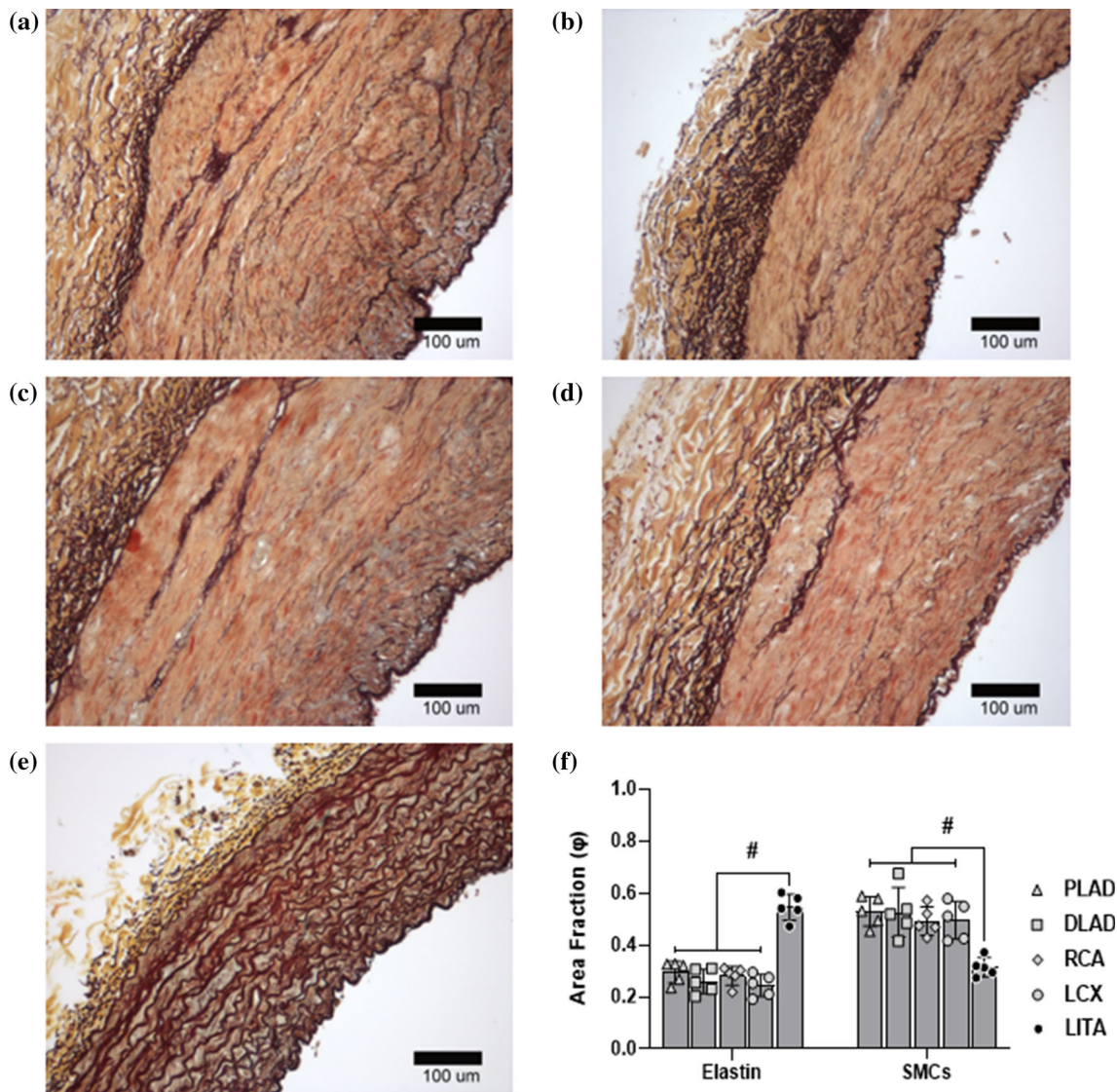


FIGURE 4. Qualitative and quantitative comparison of arterial wall composition using Movat's Pentachrome stained cross-sections. (a) PLAD; (b) DLAD; (c) RCA; (d) LCX; and (e) the third LITA segment. (f) Quantified area fractions of elastin and smooth muscle cell dyes for all arterial sections ($n = 5$, each). Statistical significance between a coronary vessel and LITA is denoted as (#) at $p < 0.05$. Mean \pm SD.

($p \leq 0.005$) than all coronary arteries (Figs. 3b and 3c, respectively).

Image thresholding using Movat's Pentachrome stain revealed that the amount of elastin found within the LITA segment was significantly greater than that of all coronary arteries; PLAD ($p < 0.001$), DLAD ($p < 0.001$), RCA (0.28 ± 0.04 , $p < 0.001$), and LCX ($p < 0.001$) (Fig. 4f). Inversely, the area fraction of smooth muscle cells within LITA was significantly less than that of all coronary arteries; PLAD ($p < 0.001$), DLAD ($p < 0.001$), RCA ($p < 0.001$), and LCX ($p < 0.001$) (Fig. 4f). The adventitial collagen area fraction of the LITA was significantly less than that of all coronary arteries ($p < 0.001$) (Fig. 5f).

Interestingly, comparisons of the mechanical properties between the coronary vessels revealed few differences. Notably, the circumferential stress of the PLAD was significantly greater than that of RCA ($p < 0.005$), while the DLAD experienced a significantly higher axial stress than the PLAD ($p = 0.001$), RCA ($p = 0.003$), and LCX ($p < 0.001$) (Figs. 3c and 3d). There were no significant histological differences found between any of the coronary vessels.

All tapering simulations converged except the RCA-RITA₁, which was omitted from the results. As a representative example, colorimetric FEA model illustrations of σ_1 and τ_w for the PLAD-LITA₃ combination are shown in Figs. 6a and 6b, respectively. The spatial plots of σ_1 across the anastomotic junction

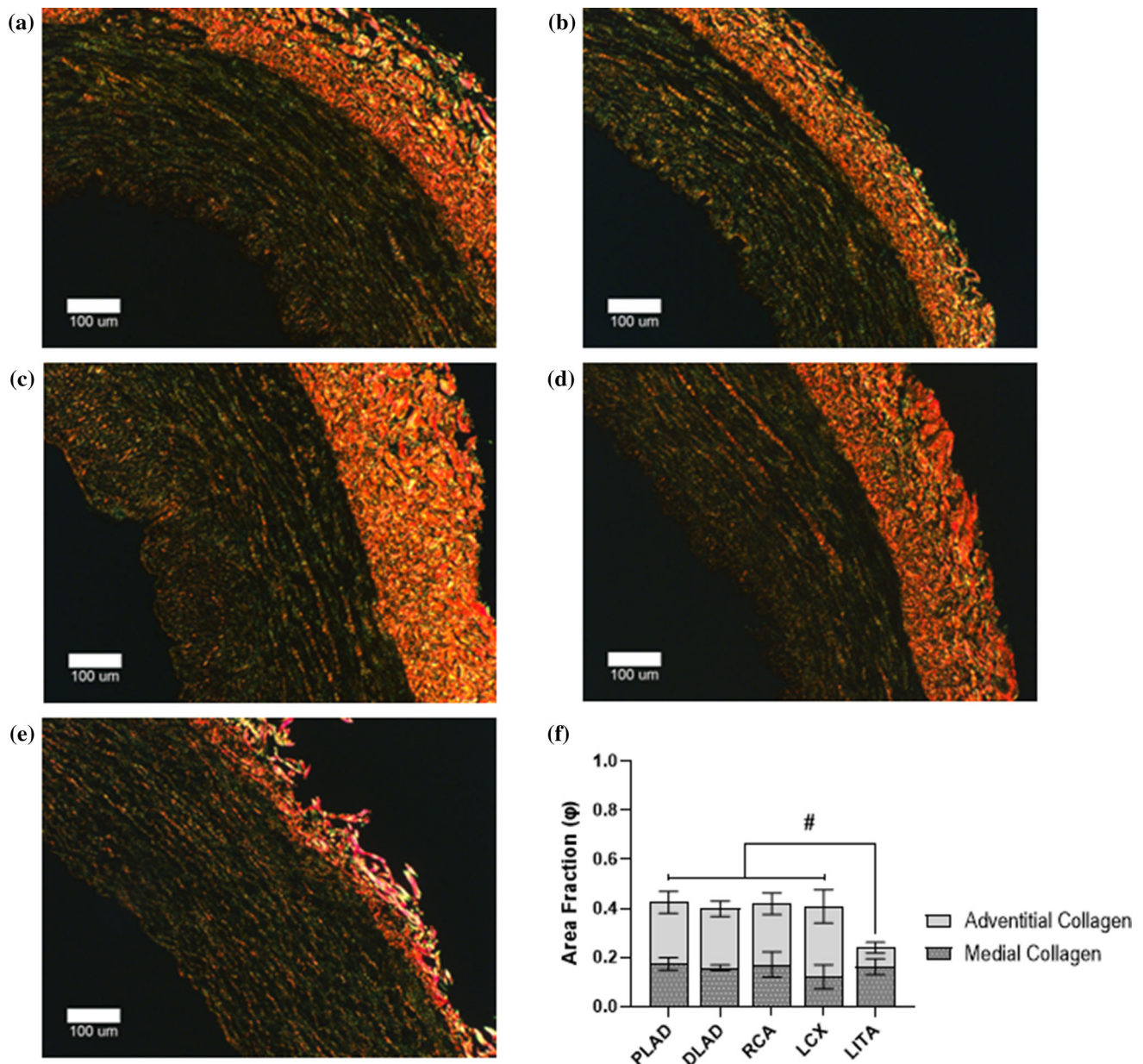


FIGURE 5. Picosirius red-stained cross-sections imaged through polarized light microscopy. (a) PLAD; (b) DLAD; (c) RCA; (d) LCX; and (e) the third LITA segment. (f) Quantified area fractions of medial and adventitial collagen birefringence ($n = 5$, each). Statistical significance between the adventitial collagen of a coronary vessel and LITA is denoted as (#) at $p < 0.05$. Mean \pm SD.

for all configurations are shown in Fig. 7; likewise, τ_w is displayed in Fig. 8. Maximum stresses for each simulation (i.e., the peak values of each curve in Figs. 7 and 8) are collated and reported in Table 3. The ITA graft segment that yielded the maximum and minimum stress values for each coronary vessel are highlighted in red and blue, respectively. Notably, for the PLAD, RCA, and LCX, the maximum σ_1 occurred when anastomosed with the LITA₁, while the DLAD, on the other hand, was highest when anastomosed to the LITA₄. Likewise, for PLAD, DLAD, and LCX, the

maximum τ_w occurred when anastomosed with LITA₄, while RCA maximum occurred when connected with RITA₄. Finally, the solid and fluid simulation outputs were normalized and averaged to create an objective function relative to the basal coronary stress values. Table 4 shows normalized values for each coronary artery in red and blue, respectively, inferring the greatest and smallest degree of deviation from the basal coronary stresses. This table reveals that the poorest overall grafting options largely follow the trends set by the first principal stress in Table 3 (LITA₁

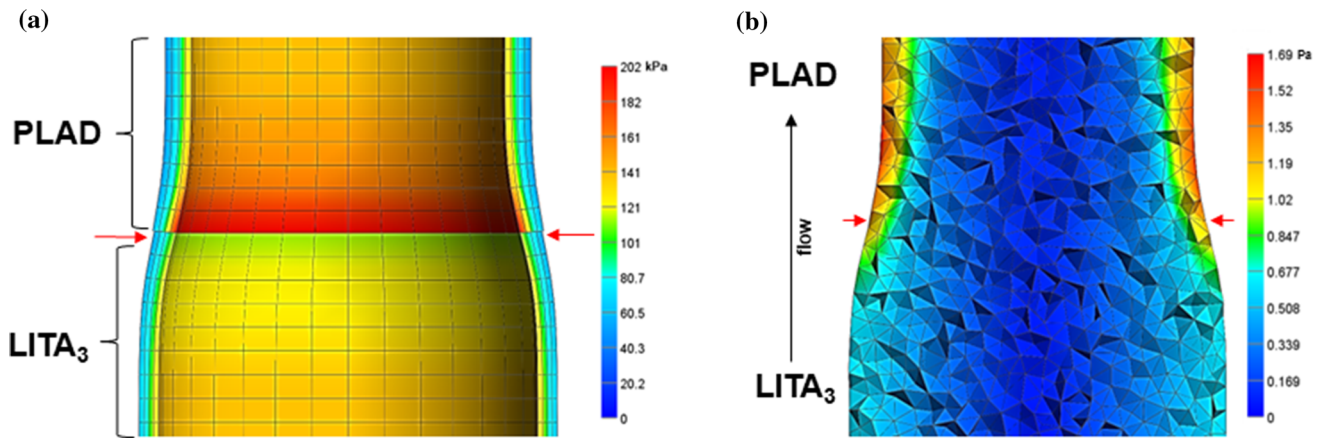


FIGURE 6. Computational analysis of PLAD-LITA₃ end-to-end anastomosis. (a) Colorimetric illustration of first principal stress (σ_1) after inflation from 0 to 100 mmHg. (b) Colorimetric illustration of fluid shear stress (τ_w) at the inflated configuration. Red arrows depict the contact region representing the anastomosis.

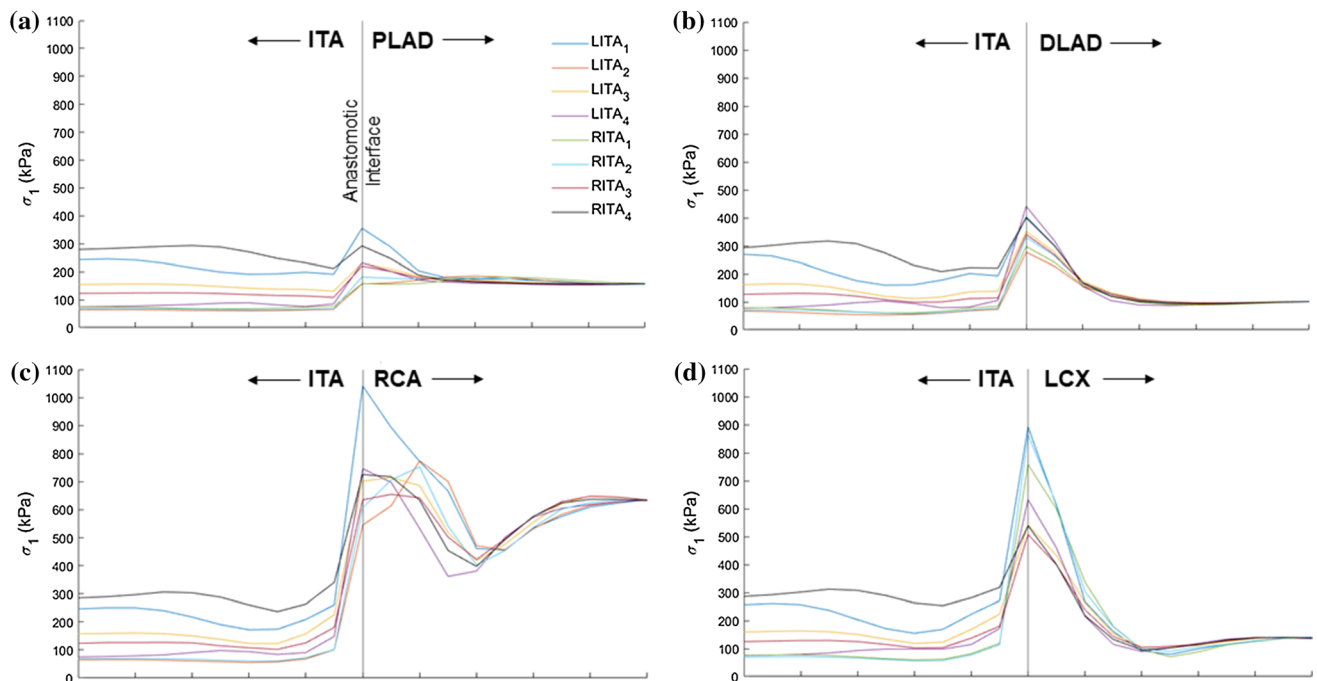


FIGURE 7. Plots of the first principal stress (σ_1) along the anastomosis for all ITA-coronary combinations. (a) ITA_x-PLAD, (b) ITA_x-DLAD, (c) ITA_x-RCA, and (d) ITA_x-LCX where x represents the respective ITA region. The vertical line represents the anastomotic junction between the two vessels.

for all except for the DLAD). The best grafting options for the LADs are LITA₂ while the best grafting options for the RCA and LCX are RITA₃ and LITA₄.

DISCUSSION

Anisodiametric and anisocompliant graft-target tissue combinations have been correlated to increased restenosis rates and premature graft failure.^{7, 17, 46} Since the joining of distinctly different anisotropic

tissues creates nonlinearities at the interface with resultant geometries that are not easily solved using standard analytical approaches, we present a histomechanical and computationally-driven objective function to assess the biomechanical responses of the different ITA grafting regions for a given coronary target. Our study provides insight into the inherent differences between these tissues and illustrates the solid mechanical and fluid dynamic consequences that arise in an end-to-end CABG anastomosis configuration.

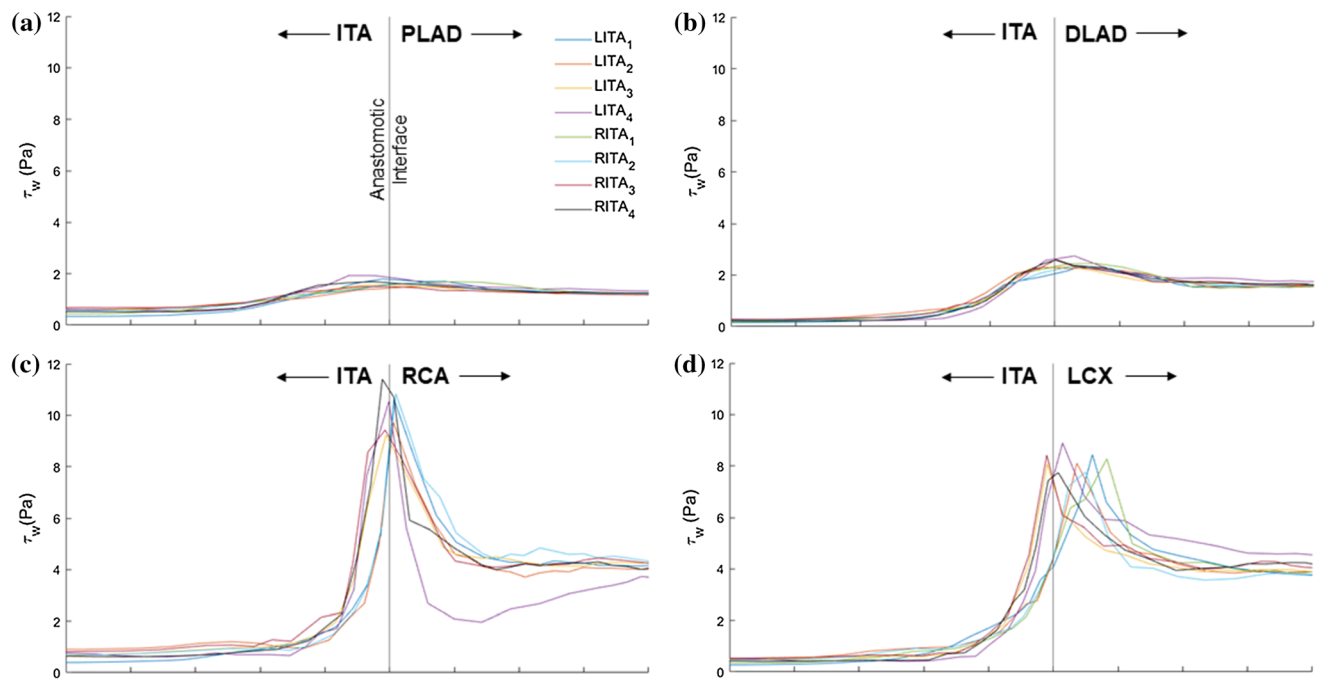


FIGURE 8. Plots of the maximum fluid shear stress (τ_w) along the anastomosis for all ITA-coronary combinations. (a) ITA_x-PLAD, (b) ITA_x-DLAD, (c) ITA_x-RCA, and (d) ITA_x-LCX where x represents the respective ITA region. The vertical line represents the anastomotic junction between the two vessels.

TABLE 3. Summary of peak simulation outputs from the solid–fluid models of all anastomosis configurations.

Maximum first principal stress [σ_1] (kPa)								
	LITA ₁	LITA ₂	LITA ₃	LITA ₄	RITA ₁	RITA ₂	RITA ₃	RITA ₄
PLAD	355.40	185.37	230.64	231.71	181.02	181.45	220.07	293.52
DLAD	403.61	277.01	350.98	441.10	297.39	329.83	340.39	399.78
RCA	1041.24	774.71	714.83	746.61		753.51	655.09	725.84
LCX	892.61	864.45	541.99	632.61	758.23	864.45	507.53	539.10
Maximum wall shear stress [τ_w] (Pa)								
	LITA ₁	LITA ₂	LITA ₃	LITA ₄	RITA ₁	RITA ₂	RITA ₃	RITA ₄
PLAD	1.79	1.50	1.58	1.93	1.69	1.63	1.50	1.69
DLAD	2.34	2.31	2.34	2.74	2.45	2.33	2.59	2.59
RCA	10.63	9.71	9.24	10.54		10.84	9.43	11.40
LCX	8.44	8.10	8.07	8.89	8.27	7.76	8.41	7.74

Maximum values in each group are highlighted in red and minimum values for each group are highlighted in blue. The gray box indicates a computational model that did not converge..

Not surprisingly, our computational analyses revealed the mechanical response across the anastomotic junction was unique for each ITA-coronary graft combination. Even though our simplified approach

uses sutureless and idealized end-to-end anastomoses, the interface still experiences high-stress concentrations due to the abrupt change in geometry and material properties. Moreover, our simulations show the peak

TABLE 4. Results of the normalized objective function for all anastomosis combinations.

	LITA ₁	LITA ₂	LITA ₃	LITA ₄	RITA ₁	RITA ₂	RITA ₃	RITA ₄
PLAD	0.926	0.387	0.529	0.723	0.477	0.447	0.463	0.732
DLAD	0.738	0.460	0.628	1	0.568	0.581	0.719	0.844
RCA	0.952	0.755	0.694	0.792		0.814	0.675	0.834
LCX	0.954	0.862	0.692	0.833	0.869	0.867	0.705	0.657

Solid–fluid simulation outputs were normalized to basal coronary mechanical and fluid dynamic values and averaged. For each coronary artery, the anastomosis configuration that resulted in the most significant deviation is shown in red, while the smallest is shown in blue.

stress values occur predominantly on the coronary side of the anastomotic junction, a finding supported by the literature that depicts the suture line as a vulnerable site for the development of intimal hyperplasia in response to mechanical mismatch with the graft.^{6, 31} This evidence supports normalizing our solid mechanical simulation outputs to the basal levels of coronary stresses rather than those of the graft tissue. For vein grafts, intimal-medial thickening occurs within the graft tissue itself.^{10, 30} However, when these vein grafts were analyzed spatially, 67% developed fibro-intimal thickening, and 33% had an atherosclerotic plaque on the proximal (aortic) side, while 96% showed fibro-intimal thickening and only 4% had an atherosclerotic plaque on the distal (coronary) side.⁴⁷ Indeed, several factors play a role in the etiology of regional graft failure, but compatibility with the anastomosing tissue is likely paramount to this process. Still, more attention needs to be given to the spatial pathology of arterio-graft disease.

Our finite element results provide a framework for optimal graft selection based on the minimization of an objective function for all graft vessels. Most of the coronary arteries matched poorest with the LITA₁ except for the DLAD. Interestingly, the DLAD exhibited the greatest axially-biased anisotropy as indicated by the pairwise contribution of axial parameters c_1^1 and c_2^1 to the total strain energy. In contrast, the PLAD had the greatest isotropic contributions to the total strain energy (parameter c , Table 1) and most potential ITA graft vessels matched extremely well with this coronary artery. Although experimental and computational tools of biomechanical analyses (i.e., how biological bodies respond to applied forces or displacements) were used in this study to predict localized stress gradients, the underlying motivation for our work was one of mechanobiology (i.e., how physical loads affect the biological output of

cells). That said, the vascular wall cells are accustomed to basal levels or “homeostatic” stresses with chronic perturbations in loading, leading to a restoration of long-term stress.^{19, 24, 33, 45} Cellular and tissue level stresses are not zero with resident vascular cells exposed to healthy multi-directional periodic loading *in vivo*. Moreover, emerging evidence supports the idea that the cells of the graft tissue are gradually replaced by the host.³⁶ For these reasons, basal values of homeostatic coronary vessel stresses were chosen as a baseline for normalization rather than values of the graft tissue. Likewise, regions of low-shear are known for atherosclerotic plaque localization and progression, but high-shear regions have also been linked to plaque progression/transformation, necrotic core progression, and increased apoptosis rates.^{14, 17, 39} Interestingly, the fluid and solid stress levels found from our computational analysis were an order of magnitude lower in the LAD than the RCA and LCX anastomoses and may be responsible, in part, for the enhanced pathological outcomes in this region.³⁷ Still, further study into regional pathologies is needed to draw a more robust conclusion.

Our approach towards estimating constitutive parameters are based on the axisymmetric deformation of anisotropic cylindrical specimens experiencing elastic deformations under pressurization and longitudinal extension thus subjecting all specimens (ITA and coronary) to the same set of conditions. Although we chose the straightest regions of the coronary vasculature possible, Saravanan *et al.* showed that the porcine circumflex artery actually undergoes bending and twisting and that omission of these deformations adds uncertainty to the analysis.⁴⁰ This observation may play a role in the disparate axial stress values displayed in Fig. 3d, but further analysis beyond the scope of the current work would be required. Overall, our analytical and computational approaches were indeed ideal-

ized. Likewise, end-to-end anastomoses are rarely implemented clinically. This configuration, however, demonstrates an axisymmetric stress field, permits clear comparisons of compliance mismatching, and enables direct interpretation of ongoing mechanobiologically-driven experimental assessments such as immunohistochemistry, ELISAs, qPCR, and Western blot analyses. An unfortunate disadvantage is that significant size discrepancies between the graft and host tissues limit potential configurations experimentally and computationally. For example, our tapered computational geometries and tied facet-on-facet contact restrictions could not be implemented for the RCA-RITA₁ combination. End-to-side, spatulated, or even fish-mouth surgical techniques could be performed to circumvent such limitations.^{7, 35} These are important for translating the current work into clinical investigations and are part of our ongoing studies. Another notable limitation was the idealized nature of the virtual anastomotic junction. In addition, there was no stress history carried over from the virtual anastomosing process to elucidate local stress gradients that arise solely from intraluminal pressurization. As a common site for surgically-induced vascular injury, the exclusion of sutures or other surgical materials (e.g., vascular clips) from our models allowed for quantification of the solid mechanical and hemodynamic stress gradients that arise solely from the gross biomechanical differences between the graft and target tissues rather than the stress concentrations around sutures.^{6, 41, 44} In fact, suture compliance matching may be as important as tissue compliance matching.⁴⁴

CONCLUSION

Using a porcine surrogate for the human central vasculature our experimental and computational analyses helped provide insight into the importance of graft tissue selection by quantifying the mechanical consequences of an idealized virtual coronary-grafting anastomosis. Based on an objective function used to stratify these tissue combinations for all converged solutions, we found the best ITA graft region for the RCA and LCX was RITA₃, and LITA₃, respectively, while the best grafting region for both PLAD and DLAD was the LITA₂. Vice-versa, the worst ITA grafting region for the PLAD, RCA, and LCX was LITA₁, while the worst region for the DLAD was LITA₄. This information provides the foundational knowledge necessary for the ongoing investigations of matched and mismatched tissue combinations that will be used to establish a link between mechanobiologi-

cally-driven inflammation and thrombosis within mismatched graft-target tissues.

ACKNOWLEDGMENTS

The authors would like to acknowledge Susan Lessner for access to the Bose mechanical testing device, histological and imaging assistance of the Instrumentation Resource Facility (IRF) at USC School of Medicine, and the computational assistance of Dr. Steve Maas and Dr. Gerard Ateshian. This research was supported by the National Science Foundation (NSF) through Research Experience for Undergraduates (REU) 1852331, NSF Civil, Mechanical and Manufacturing Innovation (CMMI) 1760906, and NSF EPSCoR OIA-1655740 Grants, and the National Institutes of Health (NIH) COBRE Pilot Project P20GM103641.

CONFLICT OF INTEREST

All authors declare that they have no conflict of interest.

REFERENCES

- ¹Andersson, M., L. Karlsson, P. A. Svensson, E. Ulfhammer, M. Ekman, M. Jernås, et al. Differential global gene expression response patterns of human endothelium exposed to shear stress and intraluminal pressure. *J. Vasc. Res.* 42:441–452, 2005. <https://doi.org/10.1159/000087983>.
- ²Azar, D., D. Ohadi, A. Rachev, J. F. Eberth, M. J. Uline, and T. Shazly. Mechanical and geometrical determinants of wall stress in abdominal aortic aneurysms: a computational study. *PLoS ONE*. 13:1–15, 2018. <https://doi.org/10.1371/journal.pone.0192032>.
- ³Azar, D., W. M. Torres, L. A. Davis, T. Shaw, J. F. Eberth, V. B. Kolachalama, et al. Geometric determinants of local hemodynamics in severe carotid artery stenosis. *Comput. Biol. Med.* 114:103436, 2019. <https://doi.org/10.1016/j.combiomed.2019.103436>.
- ⁴Baek, S., R. L. Gleason, K. R. Rajagopal, and J. D. Humphrey. Theory of small on large: potential utility in computations of fluid–solid interactions in arteries. *Comput. Methods Appl. Mech. Eng.* 196:3070–3078, 2007. <https://doi.org/10.1016/j.cma.2006.06.018>.
- ⁵Baguneid, M. S., S. Goldner, P. E. Fulford, G. Hamilton, M. G. Walker, and A. M. Seifalian. A comparison of para-anastomotic compliance profiles after vascular anastomosis: nonpenetrating clips versus standard sutures. *J. Vasc. Surg.* 33:812–820, 2001.
- ⁶Ballyk, P. D., C. Walsh, J. Butany, and M. Ojha. Compliance mismatch may promote graft–artery intimal hyperplasia by altering suture-line stresses. *J. Biomech.*

- 31:229–237, 1997. [https://doi.org/10.1016/S0197-3975\(97\)00111-5](https://doi.org/10.1016/S0197-3975(97)00111-5).
- ⁷Cavalcanti, S., and A. Tura. Hemodynamic and mechanical performance of arterial grafts assessed by numerical simulation: a design oriented study. *Artif. Organs*. 23:175–185, 1999. <https://doi.org/10.1046/j.1525-1594.1999.06217.x>.
- ⁸Chatzizisis, Y. S., A. U. Coskun, M. Jonas, E. R. Edelman, C. L. Feldman, and P. H. Stone. Role of endothelial shear stress in the natural history of coronary atherosclerosis and vascular remodeling: molecular, cellular, and vascular behavior. *J. Am. Coll. Cardiol.* 49:2379–2393, 2007. <http://doi.org/10.1016/j.jacc.2007.02.059>.
- ⁹Cunningham, K. S., and A. I. Gotlieb. The role of shear stress in the pathogenesis of atherosclerosis. *Lab. Invest.* 2005. <https://doi.org/10.1038/labinvest.3700215>.
- ¹⁰Davies, M. G., and P.-O. Hagen. Pathophysiology of vein graft failure: a review. *Eur. J. Vasc. Endovasc. Surg.* 9:7–18, 1995. [https://doi.org/10.1016/S1078-5884\(05\)80218-7](https://doi.org/10.1016/S1078-5884(05)80218-7).
- ¹¹Dobrin, P. B. Pathophysiology and pathogenesis of aortic aneurysms. Current concepts. *Surg. Clin. N. Am.* 69:687–703, 1989.
- ¹²Eberth, J. F., V. C. Gresham, A. K. Reddy, N. Popovic, E. Wilson, and J. D. Humphrey. Importance of pulsatility in hypertensive carotid artery growth and remodeling. *J. Hypertens.* 27:2010–2021, 2009. <https://doi.org/10.1097/HJH.0b013e32832e8dc8>.
- ¹³Eberth, J. F., N. Popovic, V. C. Gresham, E. Wilson, and J. D. Humphrey. Time course of carotid artery growth and remodeling in response to altered pulsatility. *Am. J. Physiol. Heart Circ. Physiol.* 299:H1875–H1883, 2010. <https://doi.org/10.1152/ajpheart.00872.2009>.
- ¹⁴Eshtehardi, P., and Z. Teng. Protective or destructive: high wall shear stress and atherosclerosis. *Atherosclerosis*. 251:501–503, 2016. <https://doi.org/10.1016/j.atherosclerosis.2016.05.046>.
- ¹⁵Fonseca, D. A., P. E. Antunes, M. J. Antunes, and M. D. Cotrim. Histomorphometric analysis of the human internal thoracic artery and relationship with cardiovascular risk factors. *PLoS ONE*. 14:1–11, 2019. <https://doi.org/10.1371/journal.pone.0211421>.
- ¹⁶Furdella, K. J., S. Higuchi, A. Behrangzade, K. Kim, W. R. Wagner, J. P. Vande, et al. In-vivo assessment of a tissue engineered vascular graft computationally optimized for target vessel compliance. *Acta Biomater.* 123:298–311, 2021. <https://doi.org/10.1016/j.actbio.2020.12.058>.
- ¹⁷Ghista, D. N., and F. Kabinejadian. Coronary artery bypass grafting hemodynamics and anastomosis design: a biomedical engineering review. *Biomed. Eng. Online*. 12:1–28, 2013. <https://doi.org/10.1186/1475-925X-12-129>.
- ¹⁸Gimbrone, M. A., J. N. Topper, T. Nagel, K. R. Anderson, and G. Garcia-Cardena. Endothelial dysfunction, hemodynamic forces, and atherogenesis. *Ann. N. Y. Acad. Sci.* 902:230–240, 2000. <https://doi.org/10.1111/j.1749-6632.2000.tb06318.x>.
- ¹⁹Gomez, D., and G. K. Owens. Smooth muscle cell phenotypic switching in atherosclerosis. *Cardiovasc. Res.* 95:156–164, 2012. <https://doi.org/10.1093/cvr/cvs115>.
- ²⁰He, G.-W. Arterial grafts for coronary artery bypass grafting: biological characteristics, functional classification, and clinical choice. *Ann. Thorac. Surg.* 67:277–284, 1999. [https://doi.org/10.1016/S0003-4975\(98\)01207-7](https://doi.org/10.1016/S0003-4975(98)01207-7).
- ²¹He, G.-W. Cautions on the use of distal internal thoracic artery and its bifurcations. *J. Thorac. Cardiovasc. Surg.* 149:1050–1, 2015. <https://doi.org/10.1016/j.jtcvs.2014.12.046>.
- ²²He, F., L. Hua, and L. J. Gao. A computational model for biomechanical effects of arterial compliance mismatch. *Appl. Bionics Biomech.* 2015. <https://doi.org/10.1155/2015/213236>.
- ²³Holzappel, G. A., T. C. Gasser, and R. W. Ogden. A new constitutive framework for arterial wall mechanics and a comparative study of material models. *J. Elast. Phys. Sci. Solids*. 61:1–48, 2000. <https://doi.org/10.1023/A:1010835316564>.
- ²⁴Humphrey, J. D. Vascular adaptation and mechanical homeostasis at tissue, cellular, and sub-cellular levels. *Cell Biochem. Biophys.* 50:53–78, 2008. <https://doi.org/10.1007/s12013-007-9002-3>.
- ²⁵Kassab, G. S., and J. A. Navia. Biomechanical considerations in the design of graft: the homeostasis hypothesis. *Annu. Rev. Biomed. Eng.* 8:499–535, 2006. <https://doi.org/10.1146/annurev.bioeng.8.010506.105023>.
- ²⁶Kostelnik, C. J., K. J. Crouse, W. Carver, and J. F. Eberth. Longitudinal histomechanical heterogeneity of the internal thoracic artery. *J. Mech. Behav. Biomed. Mater.* 116:104314, 2021. <https://doi.org/10.1016/j.jmbbm.2021.104314>.
- ²⁷Maas, S. A., B. J. Ellis, G. A. Ateshian, and J. A. Weiss. FEBio: finite elements for biomechanics. *J. Biomech. Eng.* 134(1): 011005, 2012. <https://doi.org/10.1115/1.4005694>.
- ²⁸Malota, Z., J. Glowacki, W. Sadowski, and M. Kostur. Numerical analysis of the impact of flow rate, heart rate, vessel geometry, and degree of stenosis on coronary hemodynamic indices. *BMC Cardiovasc. Disord.* 18:1–16, 2018. <https://doi.org/10.1186/s12872-018-0865-6>.
- ²⁹Marx, R., H. Clahsen, R. Schneider, H. Sons, R. M. Klein, and H. Gulker. Histomorphological studies of the distal internal thoracic artery which support its use for coronary artery bypass grafting. *Atherosclerosis*. 159:43–48, 2001. [https://doi.org/10.1016/S0021-9150\(01\)00483-X](https://doi.org/10.1016/S0021-9150(01)00483-X).
- ³⁰McKavanagh, P., B. Yanagawa, G. Zawadowski, and A. Cheema. Management and prevention of saphenous vein graft failure: a review. *Cardiol. Ther.* 6:203–223, 2017. <https://doi.org/10.1007/s40119-017-0094-6>.
- ³¹Ojha, M. Wall shear stress temporal gradient and anastomotic intimal hyperplasia. *Circ. Res.* 74:1227–1231, 1994. <https://doi.org/10.1161/01.RES.74.6.1227>.
- ³²Ootaki, Y., C. Ootaki, K. Kamohara, M. Akiyama, F. Zahr, M. W. Kopcak Jr., et al. Phasic coronary blood flow patterns in dogs vs. pigs: an acute ischemic heart study. *Med. Sci. Monit.* 14:BR193-197, 2008.
- ³³Prim, D. A., B. A. Lane, J. Ferruzzi, T. Shazly, and J. F. Eberth. Evaluation of the stress-growth hypothesis in saphenous vein perfusion culture. *Ann. Biomed. Eng.* 49:487–501, 2021. <https://doi.org/10.1007/s10439-020-02582-1>.
- ³⁴Prim, D. A., B. Zhou, A. Hartstone-Rose, M. J. Uline, T. Shazly, and J. F. Eberth. A mechanical argument for the differential performance of coronary artery grafts. *J. Mech. Behav. Biomed. Mater.* 54:93–105, 2016. <https://doi.org/10.1016/j.jmbbm.2015.09.017>.
- ³⁵Rickard, R. F., C. Meyer, and D. A. Hudson. Computational modeling of microarterial anastomoses with size discrepancy (small-to-large). *J. Surg. Res.* 153:1–11, 2009. <https://doi.org/10.1016/j.jss.2008.02.038>.
- ³⁶Row, S., H. Peng, E. M. Schlaich, C. Koenigsnecht, S. T. Andreadis, and D. D. Swartz. Arterial grafts exhibiting unprecedented cellular infiltration and remodeling in vivo:

- the role of cells in the vascular wall. *Biomaterials*. 50:115–126, 2015. <https://doi.org/10.1016/j.biomaterials.2015.01.045>.
- ³⁷Sabik, J. F., B. W. Lytle, E. H. Blackstone, P. L. Houghtaling, and D. M. Cosgrove. Comparison of saphenous vein and internal thoracic artery graft patency by coronary system. *Ann. Thorac. Surg.* 79:544–551, 2005. <https://doi.org/10.1016/j.athoracsur.2004.07.047>.
- ³⁸Sahar, G., R. Shavit, Z. Yosibash, L. Novack, M. Matsa, B. Medalion, et al. The physiologic and histologic properties of the distal internal thoracic artery and its subdivisions. *J. Thorac. Cardiovasc. Surg.* 149:1042–1050, 2015. <https://doi.org/10.1016/j.jtevs.2014.12.028>.
- ³⁹Samady, H., P. Eshtehardi, M. C. McDaniel, J. Suo, S. S. Dhawan, C. Maynard, et al. Coronary artery wall shear stress is associated with progression and transformation of atherosclerotic plaque and arterial remodeling in patients with coronary artery disease. *Circulation*. 124:779–788, 2011. <https://doi.org/10.1161/CIRCULATIONAHA.111.021824>.
- ⁴⁰Saravanan, U., S. Baek, K. R. Rajagopal, and J. D. Humphrey. On the deformation of the circumflex coronary artery during inflation tests at constant length. *Exp. Mech.* 46:647–656, 2006. <https://doi.org/10.1007/s11340-006-9036-2>.
- ⁴¹Sarkar, S., H. J. Salacinski, G. Hamilton, and A. M. Seifalian. The mechanical properties of infrainguinal vascular bypass grafts: their role in influencing patency. *Eur. J. Vasc. Endovasc. Surg.* 31:627–636, 2006. <https://doi.org/10.1016/j.ejvs.2006.01.006>.
- ⁴²van Son, J. A. M., F. Smedts, P. C. M. de Wilde, N. H. J. Pijls, L. Wong-Alcala, K. Kubat, et al. Histological study of the internal mammary artery with emphasis on its suitability as a coronary artery bypass graft. *Ann. Thorac. Surg.* 55:106–113, 1993. [https://doi.org/10.1016/0003-4975\(93\)90483-X](https://doi.org/10.1016/0003-4975(93)90483-X).
- ⁴³Taqueti, V. Sex differences in the coronary system. *Adv. Exp. Med. Biol.* 1065:257–278, 2018. <https://doi.org/10.1007/978-3-319-77932-4>.
- ⁴⁴Tiwari, A., K.-S.S. Cheng, H. Salacinski, G. Hamilton, and A. M. Seifalian. Improving the patency of vascular bypass grafts: the role of suture materials and surgical techniques on reducing anastomotic compliance mismatch. *Eur. J. Vasc. Endovasc. Surg.* 25:287–95, 2003. <https://doi.org/10.1053/ejvs.2002.1810>.
- ⁴⁵Wadey, K., J. Lopes, M. Bendeck, and S. George. Role of smooth muscle cells in coronary artery bypass grafting failure. *Cardiovasc. Res.* 114:601–610, 2018. <https://doi.org/10.1093/cvr/cvy021>.
- ⁴⁶Weston, M. W., K. Rhee, and J. M. Tarbell. Compliance and diameter mismatch affect the wall shear rate distribution near an end-to-end anastomosis. *J. Biomech.* 29:187–198, 1996. [https://doi.org/10.1016/0021-9290\(95\)00028-3](https://doi.org/10.1016/0021-9290(95)00028-3).
- ⁴⁷Yazdani, S. K., A. Farb, M. Nakano, M. Vorpahl, E. Ladich, A. V. Finn, et al. Pathology of drug-eluting versus bare-metal stents in saphenous vein bypass graft lesions. *JACC Cardiovasc. Interv.* 5:666–674, 2012. <https://doi.org/10.1016/j.jcin.2011.12.017>.

Publisher's Note Springer Nature remains neutral with regard to jurisdictional claims in published maps and institutional affiliations.

Springer Nature or its licensor (e.g. a society or other partner) holds exclusive rights to this article under a publishing agreement with the author(s) or other rightsholder(s); author self-archiving of the accepted manuscript version of this article is solely governed by the terms of such publishing agreement and applicable law.